

Eta electroproduction on nuclei in the nucleon resonance region

J. Lehr and U. Mosel

Institut für Theoretische Physik, Universität Giessen

D-35392 Giessen, Germany

(Dated: November 5, 2018)

We investigate eta electroproduction on nuclei for $Q^2 = 2.4$ and 3.6 GeV^2 in the framework of a coupled-channel BUU transport model. We analyze the importance of final state interactions and side feeding and compare with findings drawn from eta photoproduction. It is shown that in contrast to photoproduction the influence of etas stemming from secondary processes becomes important at high Q^2 .

PACS numbers: 25.30.-c, 25.30.Rw, 25.20.Lj

I. INTRODUCTION

Photon and electron induced reactions provide a useful tool to probe particle properties in the nuclear medium. In the nucleon resonance region, meson production can be used to learn about the in-medium properties of nucleon resonances. Among other processes, measurements of eta photoproduction were performed [1, 2] in order to obtain information about the $S_{11}(1535)$. This channel is particularly interesting because of the strong coupling between the eta and the $S_{11}(1535)$ in the energy region from the ηN threshold up to invariant masses of about 1.6 GeV. In photoproduction the momentum transfer and the mass of the created resonance are directly related to each other: In the vacuum, a S_{11} with pole-mass of $\mu = 1.535 \text{ GeV}$ can only be excited by a real photon with energy $E_\gamma \sim 0.787 \text{ GeV}$; inside the nucleus this condition is somewhat softened due to Fermi motion.

Only recently, we have calculated η photoproduction on different nuclei in the region of the $S_{11}(1535)$ [3]. The agreement with the available data is good when a momentum dependent resonance potential is applied. We have found collisional broadening for the S_{11} of only about 30 MeV that had almost no visible effect on the cross section. It is therefore interesting to see whether this holds over a larger range of resonance momenta. For a review of photon induced processes within our model we refer to [3, 4, 5].

In electroproduction experiments, the electron interacts with the nucleus by the exchange of a single virtual photon (one-photon exchange approximation). This yields an additional degree of freedom, because photon energy and momentum can now be chosen independently from each other. Therefore, the resonance self energy can be probed over a full range of mass and momentum. Electroproduction of mesons in the resonance region at low $Q^2 \leq 0.8 \text{ GeV}^2$ was already addressed in the framework of the coupled-channel BUU model in [5].

A disadvantage of electron induced processes is the decrease of the cross sections with increasing Q^2 . Especially the resonant structure becomes less pronounced due to the Q^2 dependence of the photocoupling helicity amplitudes (see e.g. [6]). In addition, Fermi motion becomes the more effective the larger Q^2 is [5], resulting in a smearing of the resonant structure over a wide energy range and an even stronger decrease of the cross section maxima.

In this work we calculate eta electroproduction on nuclei within a semi-classical coupled-channel BUU transport model; the same model was used in [3] to calculate photon induced eta production. In this work, we investigate eta production mechanisms in electroproduction in the kinematical regime accessible at JLab and compare with findings from eta photoproduction. This makes it possible to study the transition from low resonance momenta at $Q^2 = 0$ to larger momenta at $Q^2 = 3.6 \text{ GeV}^2$, i.e. probing the momentum regime of a pole-mass resonance from 0.8 GeV up to more than 3 GeV.

In Sec. II we briefly discuss the BUU model, our approach to the $\gamma^* N \rightarrow \eta N$ reaction and the treatment of the final state interactions (FSI). In Sec. III we qualitatively compare differences between eta photo- and electroproduction.

II. THE MODEL

We treat the electron-nucleus reaction in the one-photon exchange approximation. Therefore, the process can be described in the same way as in photoproduction. The model then contains two aspects: the reaction of the (virtual) photon with the nucleus and the treatment of the final state interactions (FSI).

A. The photon-nucleon reaction

For the elementary reaction, we assume that the photon is absorbed by a single nucleon. In the nucleon resonance region the relevant processes are

$$\gamma^*N \rightarrow P_{33}(1232), \quad \gamma^*N \rightarrow S_{11}(1535), \quad \gamma^*N \rightarrow F_{15}(1680), \quad \gamma^*N \rightarrow N\pi, \quad \gamma^*N \rightarrow N\pi\pi. \quad (1)$$

For photoproduction, also the $D_{13}(1520)$ has to be taken into account [4], but the helicity amplitude of this resonance decreases rather quickly with increasing Q^2 [6], especially compared to the S_{11} , so that its contribution to the second resonance region becomes small for $Q^2 \sim 3 \text{ GeV}^2$. Moreover, the D_{13} couples only very weakly, if at all, to the eta [7, 8]. As an input for our model, we need cross sections for the different channels displayed in (1). Unlike the case of photoproduction, where a large body of data can be exploited [4], at finite Q^2 only few processes have been measured. We present calculations for $Q^2 = 2.4$ and 3.6 GeV^2 , because we then can use the recently measured cross sections for the primary reaction $\gamma^*p \rightarrow \eta p$ by Armstrong *et al.* [9]. We assume that in the considered energy regime the reaction proceeds by the excitation and subsequent decay of a $S_{11}(1535)$ resonance; background contributions are negligible [9]. Therefore, we use a Breit-Wigner parametrization similar to that applied in eta photoproduction [3]:

$$\sigma_{\gamma p \rightarrow \eta p} = \left(\frac{k_0}{k}\right)^2 \frac{s\Gamma_\gamma(\sqrt{s})\Gamma_{S_{11} \rightarrow \eta p}(\sqrt{s})}{(s - M_{S_{11}}^2)^2 + s\Gamma_{S_{11} \rightarrow X}^2(\sqrt{s})} \frac{2m_N}{M_{S_{11}}} |A_T|^2, \quad (2)$$

with $\Gamma_\gamma = k/k_0$ and the total and partial resonance widths $\Gamma_{S_{11} \rightarrow X}(\sqrt{s})$ and $\Gamma_{S_{11} \rightarrow \eta N}(\sqrt{s})$. For the latter two we use the parametrizations from [10, 11]. $k = k(\sqrt{s})$ denotes the photon center of mass (cm) momentum and $k_0 = k(M_{S_{11}})$, where $M_{S_{11}}$ is the resonance pole mass. The transversal photocoupling helicity amplitude A_T is determined from the fit to the exclusive data in [9]; it thus contains the form factor of the resonance. The longitudinal contribution to the resonant cross section is neglected, which is a reasonable assumption [6]. The obtained values are shown in Tab. I and are in line with the findings in [9].

In Fig. 1 we show the parametrization in comparison with the data. The agreement is very good. Note that the energy dependence of the curves is strongly influenced by the energy parametrization of the resonance widths.

It is not sufficient to account only for this direct process, because via the FSI all other elementary channels may contribute to eta production. Due to the absence of data for the other exclusive channels in (1) it is difficult to determine the respective contributions unambiguously. For the total cross section $\gamma^*p \rightarrow X$ we make use of the data compilation by Brasse *et al.* [12]. The cross section $\gamma^*p \rightarrow S_{11} \rightarrow X$ can be obtained from (2) by substituting the partial decay width in the numerator with the total width:

$$\sigma_{\gamma^*p \rightarrow S_{11} \rightarrow X} = \sigma_{\gamma^*p \rightarrow S_{11} \rightarrow \eta p} \cdot \frac{\Gamma_{S_{11} \rightarrow X}}{\Gamma_{S_{11} \rightarrow \eta p}}. \quad (3)$$

The remaining resonance contributions of the $P_{33}(1232)$ and the $F_{15}(1680)$ are determined by making Breit-Wigner parametrizations according to Eq. (2). The used transversal helicity amplitudes are also displayed in Tab. I. The P_{33} amplitudes are close to those cited in [6]. For the F_{15} much larger values (factor of ~ 2) were necessary in order to saturate the whole resonant structure in the third resonance region suggested by the inclusive data in [12]. The background contributions $\gamma^*p \rightarrow N\pi$ and $N\pi\pi$ were fixed by absorbing the remaining strength after summing all contributions incoherently to the total cross section.

In the neutron sector, there is no experimental information at all. Therefore, we use the same cross sections as for the protons, except for the channel $\gamma^*n \rightarrow S_{11}$. Here we use, as in photoproduction, the relation $\sigma_n = 2/3\sigma_p$ [3, 13].

We want to stress that the data situation does not allow a more refined separation of the total cross section into the different channels. On the other hand, the very important primary eta source $\gamma^*p \rightarrow S_{11} \rightarrow \eta p$ is well under control and the total cross section also is described by our parametrization. Moreover, the details of the separation of strength into the different pionic channels do not influence the more qualitative issues we will discuss in Sect. III.

The vacuum cross sections σ_{γ^*N} discussed so far are connected to the experimentally measured cross sections for the electron-nucleon reaction. Using the Hand convention [14], we have

$$\frac{d\sigma}{d\Omega dE'} = \Gamma \cdot \sigma_{\gamma^*N} = \frac{\alpha}{2\pi^2} \frac{E'}{E} \frac{k_\gamma}{Q^2} \frac{1}{1 - \varepsilon} \cdot \sigma_{\gamma^*N}. \quad (4)$$

Here E , E' and ε are the energies of the incoming and outgoing electrons and the degree of longitudinal polarization of the virtual photons, respectively. Ω refers to the scattering angle of the electrons in the lab frame and $k_\gamma = (s - m_N^2)/(2m_N)$ denotes the equivalent photon momentum, where \sqrt{s} is the cm energy of the γ^*N pair.

In order to measure the excitation function of the $S_{11}(1535)$ as a function of the photon energy at fixed E and Q^2 , one has to vary the electron scattering angle and the energy of identified outgoing electrons. The eta data on the proton [9] were obtained at fixed electron scattering angle, so that actually a certain finite Q^2 range was covered. This was accounted for by correcting the data accordingly. We use electron energies $E = 3.2$ and 4 GeV for $Q^2 = 2.4$ and 3.6 GeV², respectively, as in [9].

The nucleons are distributed in the nucleus according to a Woods-Saxon distribution. We apply the local density approximation with local Fermi momenta to generate the momentum distribution of the nucleons. For the binding of the nucleons we use a density and momentum dependent potential described in [3]. As a result, the kinematics of the nucleons and hence the cm energy of the initial photon-nucleon pairs differ from the vacuum case.

The kinematical situation in the considered processes is such that shadowing effects in the photon-nucleus reaction are negligible.

B. The BUU model and final state interactions

The aspect of the FSI is treated within a coupled-channel BUU transport model, which is based upon the BUU equation. This equation describes the evolution of the phase space density F_i of a certain particle type i :

$$\left(\frac{\partial}{\partial t} + \vec{\nabla}_p H \cdot \vec{\nabla}_r - \vec{\nabla}_r H \cdot \vec{\nabla}_p \right) F_i(\vec{r}, \vec{p}, \mu; t) = I_{\text{coll}}[F_N, F_\pi, F_{P_{33}(1232)}, F_\eta, \dots] \quad (5)$$

The left-hand side describes the particle propagation under the influence of a Hamilton function $H = \sqrt{(\mu_i + S_i)^2 + p_i^2}$, which in the case of baryons includes an effective scalar potential S_i . Besides the nucleon, our model contains nucleon resonances and the relevant mesonic degrees of freedom π , η , ρ , ... We use the set of 29 nucleon resonances and parameters from Manley and Saleski [10]. The collisional integral on the right-hand side accounts for the coupling to the phase space densities of other particles due to reactions such as collisions, decay and resonance formation. The collision reactions are usually of binary type. The eta meson couples to the three resonances $S_{11}(1535)$, $S_{11}(1650)$ and $F_{17}(1990)$. As already described above, we only account for the first of these resonances in the γ^*N reaction. Relevant FSI for eta production may be $NR \leftrightarrow NN$, $NR \leftrightarrow NR'$, $mN \leftrightarrow R$.

The reactions at large Q^2 with large momentum transfer in the elementary reaction involve collisions in the FSI partially with invariant masses above 2 GeV. For such reactions we use the string model Fritiof [15] to determine the particle content of the final states and the kinematics. Relevant final states in the considered energy range contain mainly the η and η' along with nucleons, Δ resonances and pions. For more model details we refer to [3, 11, 16].

III. RESULTS

We now present our results for the reaction $e^{40}\text{Ca} \rightarrow e'\eta X$ for $Q^2 = 2.4$ and 3.6 GeV² and compare with eta photoproduction $\gamma^{40}\text{Ca} \rightarrow \eta X$. We do not take into account any medium modifications for resonances.

In Fig. 2 we discuss the influence of the FSI on pion and eta photo- and electroproduction. First, we focus on the calculations obtained without FSI (dashed curves). That is, only the effects of Fermi motion, Pauli blocking and nuclear binding on the elementary reaction are studied. In the case of pions (left panels) the whole resonance region is shown. It is seen that the resonant structure, clearly visible in photoproduction, is totally washed out at larger values of Q^2 . In particular, the peak of the first resonance region has disappeared. The remaining, flat contribution of the $P_{33}(1232)$ is shown as dotted curves. The behavior is caused by the strong decrease of the resonance helicity amplitudes compared to the background processes and the more effective Fermi smearing at large Q^2 . This is demonstrated in Fig. 3, where the cm energy of the primary photon-nucleon pair is shown for different values of Q^2 . Here the photon energy in each case is chosen such that a cm energy of $M_{S_{11}} = 1.535$ GeV is obtained for a nucleon at rest. It is seen that the spectrum becomes very broad for $Q^2 = 3.6$ GeV², covering actually the whole resonance region, whereas the spectrum at $Q^2 = 0$ is confined to the second resonance region. Therefore, at fixed photon energy a much wider cm energy range is probed than in photoproduction.

In eta production, the resonance peak structure of the $S_{11}(1535)$ is visible in Fig. 2 for each Q^2 value, because no other processes contribute to this channel in the absence of FSI.

When the FSI are turned on (solid curves), we observe at $Q^2 = 0$, that the curves drop for both pions and etas: The particles that stem from the elementary reaction can be absorbed. In the pionic channel this happens by collisional reactions such as $NR \rightarrow NN$ (see [4, 5]), whereas in the eta channel this is only of small importance [3]. Here the main absorption mechanism is $\eta N \rightarrow R \rightarrow \pi N$.

With increasing Q^2 , the picture changes drastically: The curves for the pions are larger than the results without FSI for photon energies $\gtrsim 2$ GeV. For $Q^2 = 3.6$ GeV² this happens already at the beginning of the first resonance region. The reason is that the particles stemming from the elementary reaction (1) are produced at larger momentum transfer ($q_\gamma \sim 2.6$ GeV for $Q^2 = 2.4$ GeV² and $q_\gamma \sim 3.3$ GeV for $Q^2 = 3.6$ GeV² on top of the S_{11} resonance peak). Therefore the background pions and decay products of the resonances are capable of producing even more particles in the FSI. This effect is missing in photoproduction, where the pion kinetic energies are not large enough at lower photon energies. The result is that the particle loss by absorption, which is of course also present at finite Q^2 , becomes dominant.

In eta production we observe the same effect. For the higher Q^2 values the curves with and without FSI lie essentially on top of each other in the threshold region. For $Q^2 = 3.6$ GeV² the effect is even more pronounced. Note also that at finite Q^2 the cross section close to the threshold is larger than in the calculations without FSI due to secondary processes. Such contributions are also absent in photoproduction.

In Fig. 4 we analyze the origin of the observed etas again for photo- and electroproduction. It is seen that with increasing Q^2 the relative importance of the primarily produced etas (from the reaction $\gamma N \rightarrow S_{11} \rightarrow \eta N$) decreases. This is partially caused by the decrease of the helicity amplitudes and the Fermi smearing already mentioned. On the other hand, the contribution of secondary etas produced in the FSI increase and become more important for $Q^2 = 3.6$ GeV². It is remarkable that the production mechanism changes to such a degree. This also influences the information content of eta production with respect to the $S_{11}(1535)$ properties in medium, because one is less sensitive to the resonances produced in the first reaction.

In Fig. 5 we discuss the different sources the detected eta actually stem from. The processes γN , πN , $\eta N \rightarrow S_{11}$ and $BB \rightarrow S_{11}N$ denote etas resulting from the decay of S_{11} resonances that were produced in such reactions. The 'high energy' contributions denote etas resulting from baryon-baryon or baryon-meson collisions at larger energies determined by the Fritiof model either directly or by the decay of S_{11} and η' resonances produced in such events or elastic scattering at higher energies. We see that the main contribution still consists of etas that did not get absorbed and re-emitted after their first production via the S_{11} decay. However, as already described above, at higher Q^2 secondary processes become more important, especially the high energy contributions and reactions from $\pi N, \eta N \rightarrow S_{11}$. The latter are also responsible for the subthreshold contributions for energies below the threshold of the $\gamma N \rightarrow S_{11}$ channel.

IV. SUMMARY

We have calculated eta production in photon and electron induced reactions on nuclei for several values of Q^2 . This is of particular interest, because at large Q^2 the physics of the resonance region (i.e. reactions with invariant masses below 2 GeV) is mixed with FSI at larger energies than encountered in photoproduction.

We have found that the FSI mechanisms change with increasing Q^2 from an essentially absorptive character at $Q^2 = 0$ to a source of relevant contributions. This is due to the increasing momentum transfer in the elementary reaction and an opening of secondary eta production channels in the FSI. It is clear that the inclusion of such side-feeding effects is important for the interpretation of eta electroproduction in terms of possible in-medium modifications of the $S_{11}(1535)$ resonance. Furthermore, we have found that the FSI also lead to an increase of the cross sections for pion and eta production. A similar effect has been seen in high-energy photo production of K^+ [16] and of ρ mesons [17] on nuclei.

ACKNOWLEDGMENTS

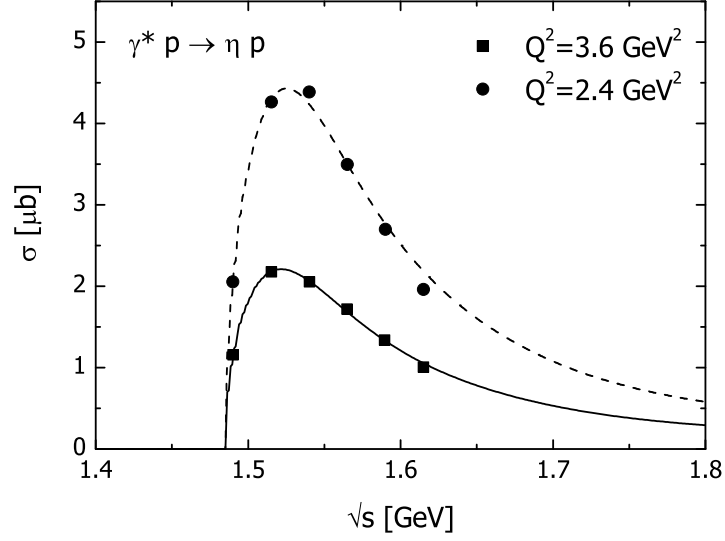
This work was supported by DFG.

-
- [1] B. Krusche *et al.*, Phys. Rev. Lett. **74**, 3736 (1995).
 - [2] T. Yorita *et al.*, Phys. Lett. **B476**, 226 (2000).
 - [3] J. Lehr, M. Post, U. Mosel, nucl-th/0306024, submitted to Phys. Rev. C
 - [4] M. Effenberger, A. Hombach, S. Teis, U. Mosel, Nucl. Phys. **A614**, 501 (1997).
 - [5] J. Lehr, M. Effenberger, U. Mosel, Nucl. Phys. **A671**, 503 (2000).
 - [6] P. Stoler, Phys. Rep. **226**, 103 (1993).

- [7] Particle Data Group, Review of Particle Physics, K. Hagiwara *et al.*, Phys. Rev. **D66**, 010001 (2002).
- [8] G. Penner, U. Mosel, Phys. Rev **C66**, 055212 (2002).
- [9] C.S. Armstrong *et al.*, Phys. Rev. **D60**, 052004 (1999).
- [10] D.M. Manley, E.M. Saleski, Phys. Rev. **D45**, 4002 (1992).
- [11] M. Effenberger, E.L. Bratkovskaya, U. Mosel, Phys. Rev. **C60**, 044614 (1999).
- [12] F.W. Brasse, W. Flauger, J. Gayler, S.P. Goel, R. Haidan, M. Merkwitz, H. Wriedt, Nucl. Phys. **B110**, 413 (1976).
- [13] B. Krusche *et al.*, Phys. Lett. **B358**, 40 (1995).
- [14] L.N. Hand, Phys. Rev **129**, 1834 (1963).
- [15] B. Andersen, G. Gustafson, Hong Pi, Z. Phys. **C57**, 485 (1993).
- [16] M. Effenberger, U. Mosel, Phys. Rev. **C62**, 014605 (2000).
- [17] T. Falter, K. Gallmeister, U. Mosel, Phys. Rev. **C67**, 054606 (2003).

TABLE I: Transversal helicity amplitudes A_T for the resonances.

Q^2 [GeV ²]	$A_T(P_{33}(1232))$ [GeV ^{-1/2}]	$A_T(S_{11}(1535))$ [GeV ^{-1/2}]	$A_T(F_{15}(1680))$ [GeV ^{-1/2}]
2.4	0.0688	0.0569	0.0674
3.6	0.0316	0.0401	0.0512

FIG. 1: Parametrization of the elementary process $\gamma^* p \rightarrow \eta p$ for $Q^2 = 2.4$ and 3.6 GeV² according to Eq. (2). The data are taken from [9].

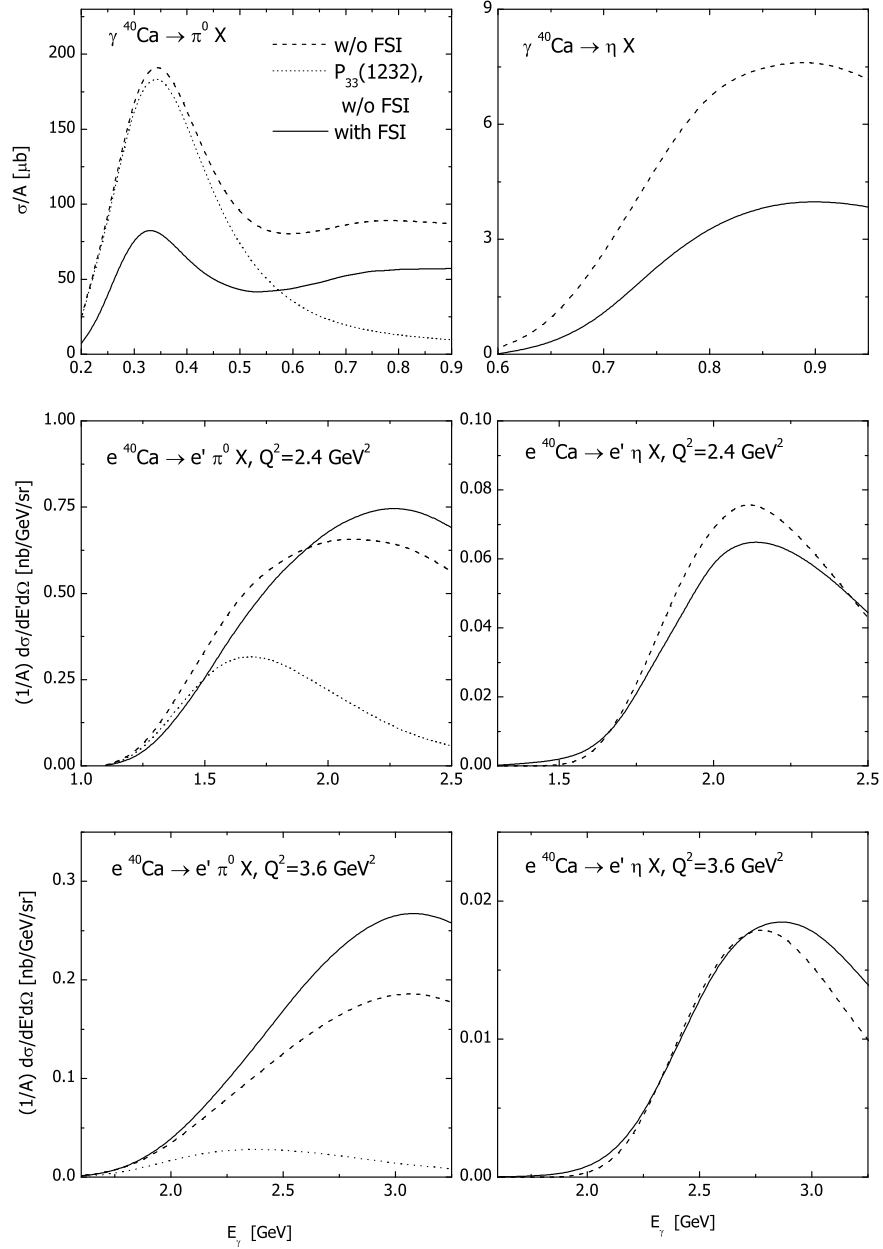


FIG. 2: Pion and eta production on Calcium. The top panels show photoproduction results, the lower ones results for electroproduction at the given Q^2 values. The solid and dashed lines show calculations with and without FSI, respectively. The dotted lines visualize the contribution of the $P_{33}(1232)$ to the cross sections without FSI.

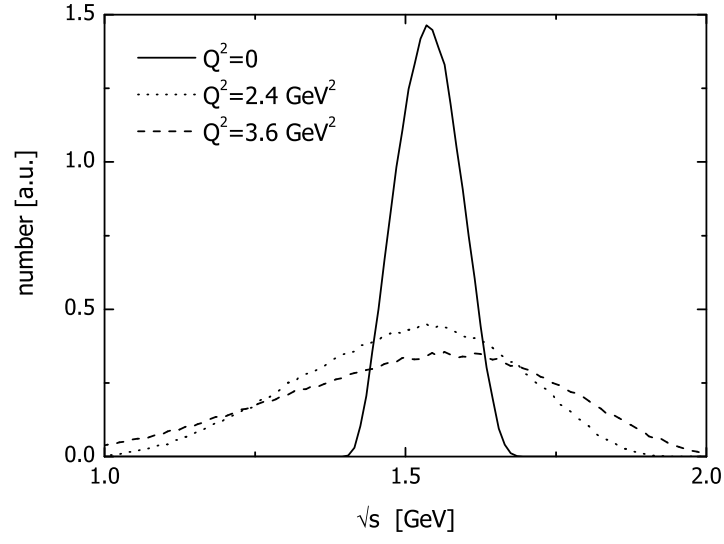


FIG. 3: \sqrt{s} spectra of the elementary γN pairs for different Q^2 . The respective photon energies were chosen such that a resonance with mass $\mu = \sqrt{s} = 1.535$ GeV is excited on a nucleon at rest.

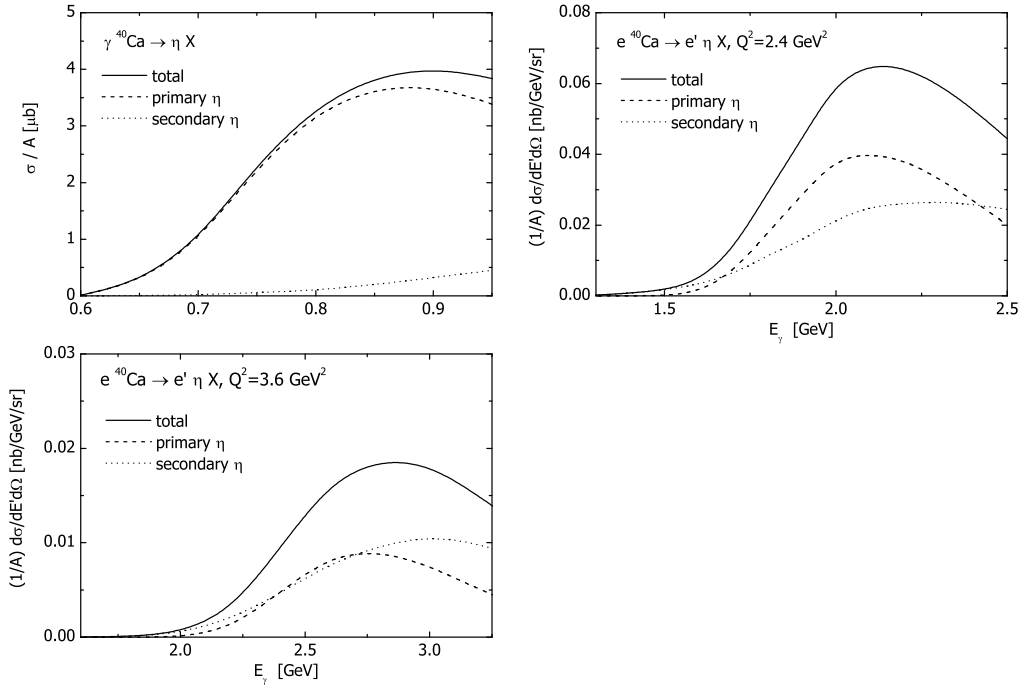


FIG. 4: Contributions from primary and secondary etas to the cross section on Calcium for different values of Q^2 .

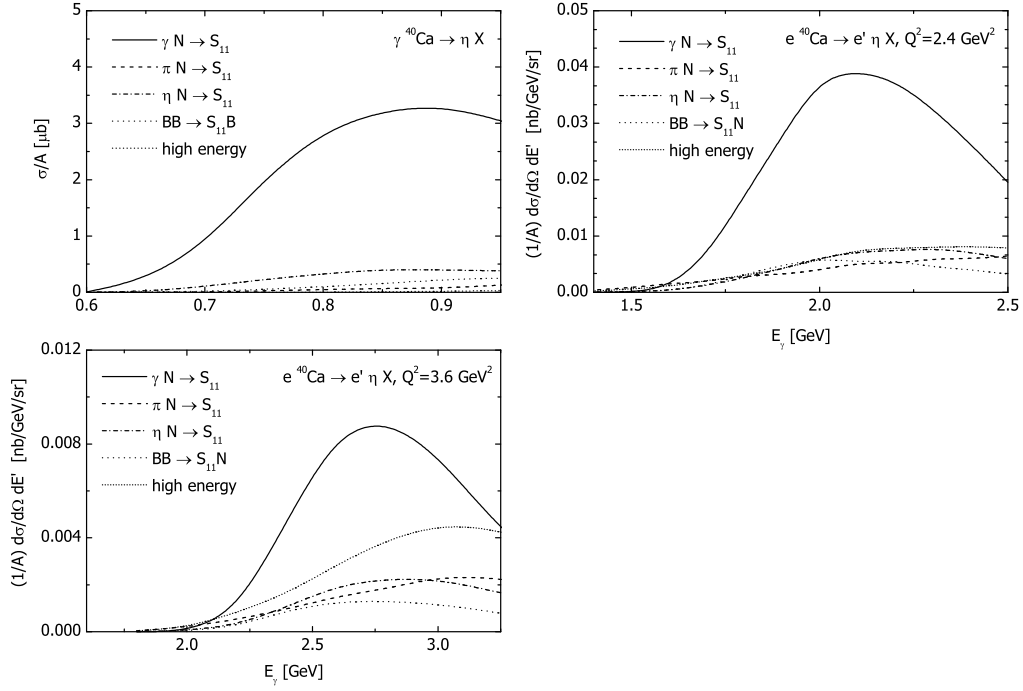


FIG. 5: Contributing channels for eta photo- and electroproduction on Calcium. The detected etas stem either from the decay of S_{11} resonances produced in the reactions given in the legend or from high energy reactions. The solid line in each case is the same as the dashed curve in Fig. 4, whereas the other curves depict the secondary production channels.